Boeckers, Hannah ; Mues, Martin Philipp ; Bredehöft, Jan Hendrik ; Swiderek, Petra

# Electron-induced hydroamination of ethane as compared to ethene: implications for the reaction mechanism

Journal Article as: peer-reviewed accepted version (Postprint)

DOI of this document*(secondary publication): https://doi.org/10.26092/elib/3708

Publication date of this document: 19/02/2025

* for better findability or for reliable citation

Recommended Citation (primary publication/Version of Record) incl. DOI:

Electron-induced hydroamination of ethane as compared to ethene: implications for the reaction mechanism
H Boeckers, MP Mues, JH Bredehöft, P Swiderek
Physical Chemistry Chemical Physics 26 (3), 2140-2152
https://doi.org/10.1039/D3CP04840C

# Electron-induced hydroamination of ethane as compared to ethene: Implications for the reaction mechanism

Hannah Boeckers,[a] Martin Philipp Mues,[a,b] Jan Hendrik Bredehöft[a] and Petra Swiderek*[a]

The properties of carbonaceous materials with respect to various applications are enhanced by incorporation of nitrogen-containing moieties like, for instance, amino groups. Therefore, processes that allow to introduce such functional groups into hydrocarbon compounds are of utmost interest. Previous studies have demonstrated that hydroamination reactions which couple amines to unsaturated sites within hydrocarbon molecules do not only proceed in the presence of suitably tailored catalysts but can also be induced and controlled by electron irradiation. However, studies on electron-induced hydroaminations so far were guided by the hypothesis that unsaturated hydrocarbons are required for the reaction while the reaction would be much less efficient in the case of saturated hydrocarbons. The present work evaluates the validity of this hypothesis by post-irradiation thermal desorption experiments that monitor the electron energy-dependent yield of ethylamine after electron irradiation of mixed $C_2H_4$:$NH_3$ and $C_2H_6$:$NH_3$ ices with the same composition and thickness. The results reveal that, in contrast to the initial assumption, ethylamine is formed with similar efficiency in both mixed ices. From the dependence of the product yields on the electron energy, we conclude that the reaction in both cases is predominantly driven by electron ionization of $NH_3$. Ethylamine is formed via alternative reaction mechanisms by which the resulting $NH_2^{\bullet}$ radicals add to $C_2H_4$ and $C_2H_6$, respectively. The similar efficiency of amine formation in unsaturated and saturated hydrocarbons demonstrates that electron irradiation in presence of $NH_3$ is a more versatile tool for introducing nitrogen into carbonaceous materials than previously anticipated.

## 1. Introduction

Carbonaceous materials are relevant to a wide range of applications including, among others, water treatment [1], $CO_2$ capture [2-9], catalysis [10-12], novel electrode materials [13], and sensing [14-15]. Their properties can be tuned and enhanced by incorporation of heteroatoms [1-16]. Nitrogen-doping, for instance, increases the binding strength towards diverse molecules such as contaminants [1], $CO_2$ [2,3], or $H_2O$ [15]. It also changes the electrical conductivity of a carbonaceous material [10,13] or optical properties like the fluorescence efficiency [17]. Furthermore, the activity of the material towards electrocatalytic reactions of oxygen is enhanced by active nitrogen defect sites [10,11] offering the prospects to develop metal-free catalysts [12]. Due to these promising perspectives, new routes towards incorporation of nitrogen in carbonaceous materials and a profound understanding of how to control these reactions are of utmost interest.

Among the different functional groups that may be formed upon uptake of nitrogen into a carbonaceous material, amine functionalization is particularly versatile. Because of their capability to act as complexation agent and to involve in hydrogen-bonding, amino groups (-$NH_2$) can remove a variety of contaminants from water [18] and are particularly efficient with regards to $CO_2$ adsorption capacity [7,8,19]. However, surface-bound amino groups are also excellent functionalities for covalent attachment of molecular entities. This is, for instance, exploited in molecular layer deposition (MLD) processes that allow for a precise layer-by-layer deposition of material on surfaces [20] and is also used to immobilize biomolecules on surfaces [21].

Amino groups on surfaces can be prepared by electron beam processes, offering the prospect of spatial control in the preparation and thus the possibility to fabricate chemically patterned surfaces. For example, such a process, termed chemical lithography, has been demonstrated using self-assembled monolayers (SAMs) prepared from aromatic molecules with terminal nitro (-$NO_2$) groups [21,22]. Electron irradiation of these SAMs cleaves C-H and N-O bonds which initiates the conversion of nitro to amino groups [22]. As an alternative approach, the electron-induced reaction between an unsaturated hydrocarbon and $NH_3$ also leads to amine functionalization [23-25]. Such reactions, in which $NH_3$ adds to the double bond of the hydrocarbon yielding a saturated amine, are termed hydroaminations. Electron-induced hydroamination reactions have been demonstrated both in mixed ice layers of $NH_3$ and ethene ($C_2H_4$) or similar small reactants [23,24] and on the surface of a self-assembled alkenethiol monolayer with terminal CC double bond [25].

Thermally induced hydroamination reactions are subject to a substantial activation barrier because both reactants possess a large

[a] Institute for Applied and Physical Chemistry (IAPC), Fachbereich 2 (Chemie/Biologie), University of Bremen, Leobener Str. 5 (NW2), 28359 Bremen, Germany.
[b] Paderborn University, Institute for Photonic Quantum Systems (PhoQS), Warburger Str. 100, 33098 Paderborn, Germany.
† Electronic Supplementary Information (ESI) available:
See DOI: 10.1039/x0xx00000x

electron density when in their electronic ground states and therefore repel each other. In this situation, electron-withdrawing catalysts are usually employed to enhance the reaction rate [26]. The same effect can be achieved by electron ionization of one of the reaction partners. In fact, calculations predict that the hydroamination is a downhill process once an aggregate containing the reaction partners is transferred to the cation state by ionization [27]. Furthermore, the amine yield as function of electron energy shows a typical threshold behavior at energies near the lowest ionization energy of the reactants [24]. Therefore, the reaction was initially proposed to follow a cation-driven mechanism as shown in Scheme 1 for the example of $C_2H_4$ and $NH_3$ [23,27]. According to this most simple view [23], ionization of one of the reactants leads to an attractive interaction and thus to formation of a bond between $NH_3$ and a carbon atom involved in the double bond. Subsequent H migration and neutralization of the cationic product by a thermalized electron then leads to the amine product. In a refined view [27] represented by Scheme 2, the presence of an aggregate of several $NH_3$ molecules facilitates H migration by proton transfer from an ionized $NH_3^{\bullet+}$ to an adjacent neutral $NH_3$ yielding an $NH_2^{\bullet}$ radical and the stable $NH_4^+$ cation. The $NH_2^{\bullet}$ radical can add to the double bond of the hydrocarbon reactant while bond reorganization within the H-bonding network of the $NH_3$ aggregate upon capture of a thermalized electron can transfer an H atom to the second carbon atom involved in the double bond.

The view that the electron-induced hydroamination reaction proceeds only by the mechanisms presented in Schemes 1 and 2 which require the presence of a double bond in the hydrocarbon reactant was recently challenged by a study on the electron-driven incorporation of N in carbonaceous deposits [15]. The deposits were prepared by electron irradiation of condensed layers of different precursor molecules ranging from a simple aliphatic compound to a metal complex with cyclopentadienyl ligand. Despite the anticipated

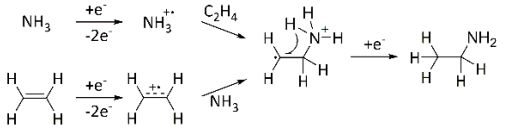

**Scheme 1.** Electron-induced hydroamination reaction between $NH_3$ and $C_2H_4$ resulting from ionization of one of the reactants. Figure adapted from [23].

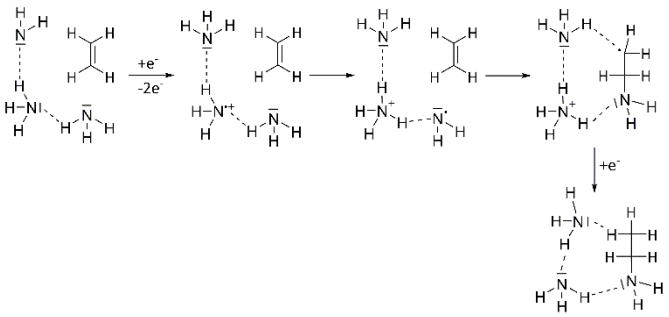

**Scheme 2.** Electron-induced hydroamination of $C_2H_4$ assisted by proton transfer between two $NH_3$ molecules resulting from ionization and by further H migration within the hydrogen bond network of an $NH_3$ aggregate. Figure adapted from [27].

varying amount of unsaturated carbon in the thus produced carbonaceous materials, the uptake of N upon electron irradiation in presence of $NH_3$ was similar in all cases [15]. This prompted the present study which compares the efficiency of hydroamination reactions of an unsaturated hydrocarbon, represented herein by $C_2H_4$, to that of the saturated reactant ethane ($C_2H_6$). The aim was to identify additional reaction pathways as compared to Schemes 1 and 2 that would allow $NH_3$ to form amines with saturated hydrocarbons. We note that such insight regarding electron-induced chemistry is not only relevant to the preparation of functional materials and surfaces as outlined above. It also helps to unravel how larger molecules can be formed in space during cosmic-ray induced processing of astrochemical ices [28,29].

Aiming at mechanistic understanding of the electron-induced reactions with $NH_3$ that lead to incorporation of N into saturated as compared to unsaturated hydrocarbons, our study investigates, for ice mixtures of either $C_2H_6$ or $C_2H_4$ with $NH_3$, the dependence of the amine product yield on the electron energy used for irradiation ($E_0$). For reference, product formation was also studied in the pure reactants. The dependence of the product yield on $E_0$ gives evidence of the type of electron interaction with the reactants that initiates the formation of new bonds between two reactant molecules [30]. More specifically, electron attachment (EA), which yields the radical anion of a reactant, as well as dissociative electron attachment (DEA), which results in an anion and at least one neutral fragment, both occur within well-defined energy ranges named resonances. The yields of products formed by reactions of intermediates resulting from EA and DEA thus show pronounced maxima at specific energies. In contrast, a threshold behavior is characteristic of neutral dissociation (ND) into radical fragments as well as of electron ionization (EI) resulting in the radical cation of a reactant and dissociative ionization (DI) into a cation and at least one neutral fragment. Maxima in the product yields at specific energies or thresholds for product formation thus give insight into the mechanisms of the investigated electron-induced reaction.

In all experiments, thermal desorption spectrometry (TDS) was performed to monitor the formation of larger products in the ice layers during electron irradiation with energies ranging from 3 eV to 20 eV. In the case of pure $NH_3$ ice, hydrazine ($N_2H_4$) was monitored while the formation of C4 hydrocarbons ($C_4H_{10}$, $C_4H_8$, and $C_4H_6$) was studied in the cases of pure $C_2H_4$ and $C_2H_6$. Finally, ethylamine and C4 hydrocarbons were detected following electron irradiation of mixed $C_2H_4$:$NH_3$ and $C_2H_6$:$NH_3$ ices. The results reveal that the efficiency of ethylamine formation is surprisingly similar in the two mixed ices. The energy dependences of the product yields together with a comprehensive survey of reference data indicate that EI of $NH_3$ is the electron-molecule interaction that initiates amine formation in both mixed ices. Based on this insight, the reaction mechanisms leading to the final product ethylamine are discussed.

## 2. Experimental

**Thermal desorption spectrometry**

Electron-induced reactions of $NH_3$ (Linde, >99%) with $C_2H_6$ (Air Liquid, 99.95 Vol%) and with $C_2H_4$ (Air Liquid, 99.95 Vol%) were studied by thermal desorption spectrometry (TDS). All experiments

were performed in an ultra-high vacuum (UHV) chamber with a base pressure below $1 \times 10^{-9}$ mbar as described previously [27]. The individual reactants or binary mixtures of $NH_3$ with either $C_2H_6$ or $C_2H_4$ were leaked from a gas handling manifold into the vacuum chamber and condensed on a polycrystalline Ta substrate which was cooled to a temperature of ~35 K by a closed-cycle helium cryostat. The amounts of reactants introduced to the UHV chamber were monitored with a capacitance manometer (MKS Baratron type 622B) that recorded the pressure drop in the gas handling manifold in units of mTorr. For TDS experiments, the sample was heated from 35 K to 450 K with a heating rate of 1 K/s while recording up to four selected m/z values. Afterwards, the sample temperature was held at 450 K for another two minutes to remove residual species from the sample holder. Neutral species that desorbed during this procedure were measured using a quadrupole mass spectrometer (QMS) residual gas analyzer (RGA 200, Stanford Research Systems) operating with electron ionization at an energy of 70 eV. For analysis, the TDS curves were smoothed using a Savitzky-Golay filter with a window length of 9 or 11 using a polynomial function of the second degree. The smoothed spectra were baseline-corrected and the desorption signals integrated using the trapezoidal rule.

The surface coverage of the adsorbed molecular layers was estimated from TDS data obtained by leaking varying amounts of vapor onto the Ta substrate. Such data typically show an evolution with increasing gas dose from a higher-temperature desorption peak at monolayer coverage to a multilayer adsorbate with well-defined peak maximum but continuously increasing intensity [31]. In the case of $NH_3$, a multilayer desorption signal was reported to emerge on different metal surfaces after formation of a bilayer [32]. In the present study, this transition occurred when a gas dose of $NH_3$ corresponding to a pressure drop of 6 mTorr in the manifold was exceeded (ESI,† Fig. S1), indicating that a gas dose around 3 mTorr is required to deposit one monolayer of $NH_3$. A pressure drop of 28 mTorr was used to prepare pure $NH_3$ ices, corresponding consequently to a thickness of roughly 9 monolayers. The thickness calibration for $NH_3$ was also used to estimate the thickness of hydrocarbon and mixed ice layers by considering the vapour mixture required to achieve a 1:1 composition of the mixed ices as detailed further on.

Mixtures of the reactants were prepared in the gas handling manifold prior to leaking of the gas. Due to the particular affinity of $NH_3$ to adsorb on the stainless steel walls of the inlet tube, the mixing ratio in the manifold does not necessarily translate into the same composition of the condensed layer. Therefore, the amounts of the two reactants in the manifold were adjusted to achieve a targeted composition. The composition of the condensed layer was deduced from the integrated TDS signals for characteristic m/z values of the two reactants, namely, m/z 17 for $NH_3$ and m/z 28 or m/z 30 for $C_2H_4$ or $C_2H_6$, respectively. Reproducibility of these integrated signals was verified by repeating the TDS experiment several times. We note that the absolute numerical values of these integrals are given in the figures to be able to compare the production of larger hydrocarbons obtained in pure $C_2H_4$ or $C_2H_6$ ices and in the mixed ices with $NH_3$. The gain factor of the continuous dynode electron multiplier (channeltron) used in the QMS was thus kept constant. The TDS peak areas derive from the MS signal multiplied by the time. For simplicity, however, we denoted these values as arbitrary units (arb. units).

To convert TDS peak areas obtained for characteristic m/z values to relative amounts of the reactants, the efficiency of formation of the ions with those particular m/z values from their parent compounds must be known. This efficiency is given by the partial ionization cross section (PICS) of a particular ion which derives from the total ionization cross section (TICS) multiplied by the fractional contribution of this particular ion within the mass spectrum, taken from [33], of the parent compound. TICS refer to the cross sections for electron ionization of the intact parent compounds while the latter quantity is simply the intensity of a single m/z value in a mass spectrum recorded with electron ionization at 70 eV divided by the sum of the intensities of all mass peaks [27]. The TICS at 70 eV were calculated as described further on. This resulted in TICS of 3.47 $Å^2$ for $NH_3$, 5.03 $Å^2$ for $C_2H_4$, and 7.22 $Å^2$ for $C_2H_6$ as well as PICS at 70 eV of 1.82 $Å^2$ for m/z 17 from $NH_3$, 2.17 $Å^2$ for m/z 28 from $C_2H_4$, and 0.87 $Å^2$ for m/z 30 from $C_2H_6$. The integrated TDS peaks were thus corrected by the PICS for the characteristic m/z values of the individual compounds to obtain the relative amounts of the two reactants in the condensed layer.

Most experiments were performed on condensed layers which contained equal amounts of hydrocarbon and $NH_3$, denoted as 1:1. All ratios of the amounts of the reactants in the mixture are stated within a margin of error of 15%. The hydrocarbon to $NH_3$ ratio in the manifold required to prepare layers with composition 1:1 was 1:(1.4±0.2). This gas mixture was leaked onto the substrate until a pressure drop of 30 mTorr in the manifold was obtained. The leaked amount of vapour thus contained (17.5±1.0) mTorr $NH_3$ and (12.5±1.0) mTorr hydrocarbon. Based on the above thickness estimate, this produced a coverage of the order of 6 monolayers of $NH_3$. Considering the 1:1 composition within the layer as derived from the TDS data, an equal amount of hydrocarbon was deposited, leading to a total thickness of 12 monolayers when assuming that the two reactants have a similar size. From this, we also derive that gas doses of roughly 2 mTorr are required to deposit a monolayer of $C_2H_6$ or $C_2H_4$. Pure layers of the hydrocarbons were prepared by leaking the gas until a pressure drop of 20 mTorr was reached, which thus resulted in an estimated thickness of about 10 monolayers.

To study the effect of the mixing ratio on the product yields, the amounts of the hydrocarbons condensed on the substrate as derived from TDS were kept approximately constant at 6 monolayers (+-20%) while the amount of $NH_3$ was varied to achieve the different targeted mixing ratios within the condensed layers. Again, the relative amounts of the reactants for a given gas mixture were verified by evaluating the desorption peak areas of both compounds for repetitive TDS experiments. The layer thickness in these experiments was again estimated based on the monolayer equivalent of 3 mTorr for $NH_3$ deduced above. It increased from roughly 8 to 24 monolayers when the amount of $NH_3$ was increased to obtain $NH_3$:hydrocarbon mixing ratios within the range between 1:4 and 3.5:1.

**Electron irradiation**

After the targeted mixing ratio in the condensed layers was reproducibly established, electron irradiation experiments were performed. A commercial electron source (STAIB NEK-150-1) with an

energy resolution of 0.5 eV was used for irradiation with $E_0$ ranging between 4 eV (3 eV for pure $NH_3$ ice) and 20 eV. The electron exposures per sample area (total area 2.8 $cm^2$) were determined with a picoamperemeter by measuring the current transmitted through the ice layer and integrating this signal over time. During irradiation, electron-stimulated desorption (ESD) was routinely monitored for selected m/z ratios. Representative data are presented in the ESI,† (Figs. S2 and S3). After irradiation, TDS experiments were performed for characteristic m/z values of anticipated reaction products ethylamine (m/z 45), hydrazine (m/z 29-32), and different hydrocarbons with four carbon atoms (C4 hydrocarbons), namely, butane ($C_4H_{10}$), butene ($C_4H_8$), and butadiene ($C_4H_6$). The m/z values 58, 56, and 54 as well as 43, 41, and 39 were used to monitor C4 products as further discussed in the Results and Discussion section. Product formation was derived from the integrated TDS signals at these m/z values that were measured as function of electron exposure and electron energy. Error bars for these integrals represent the standard deviation within each particular series of TDS measurements as obtained from typically three repetitions of a particular experiment with the same parameters. The margin of error of $E_0$ is 0.5 eV and the electron doses were measured within a margin of error of 5 μC/$cm^2$.

**Calculations**

The TICS were estimated using the binary-encounter-Bethe (BEB) model [34,35]. The model requires the binding energy as well as kinetic energy for all electrons. These were calculated at the B3LYP(6-311++G(d,p)) level of theory using the ORCA5 [36,37] software package and then normalized to experimental values for the ionization energy as taken from the NIST chemistry webbook database [38,39]. The resulting TICS were also compared to previous experimental data [40-43] which reveals an overall reasonable agreement with deviations mostly within the error margins of the ice compositions as estimated above (ESI,† Fig. S4).

## 3. Results and discussion

The TDS experiments described herein compare the efficiency of electron-driven reactions in mixed $C_2H_4$:$NH_3$ and $C_2H_6$:$NH_3$ ices with particular focus on the formation of ethylamine. As reference, the pure reactants $NH_3$, $C_2H_4$, and $C_2H_6$ were also studied. In the latter case, the formation of hydrazine ($N_2H_4$) or C4 hydrocarbons ($C_4H_{10}$, $C_4H_8$, and $C_4H_6$), respectively, gives evidence that the reactants are converted to a reactive state by electron irradiation. The results for the individual reactants and the mixtures are detailed in the following sections. In each case, the products were first identified at an $E_0$ well above the ionization threshold where the reactions are particularly efficient. Product yields were then measured as function of electron exposure. This served to identify an exposure that allowed to measure the characteristic TDS signals with a sufficiently high intensity to be quantified but that was still within or near the range where the product yield increases linearly. Finally, the product yields were measured as function of $E_0$ for the thus determined exposures. This ensured that only small amounts of the reactants were consumed so that the product yields reflect the energy dependence of the reaction rates [27].

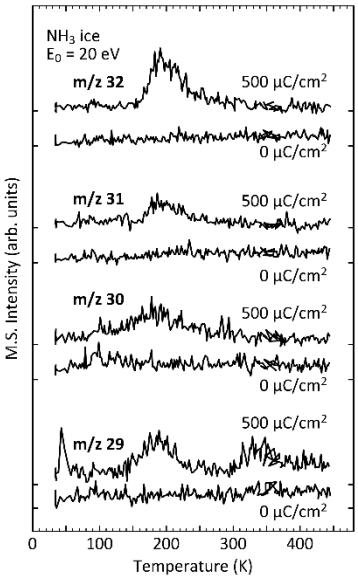


**Fig. 1.** TDS curves obtained for m/z 29, 30, and 32 from $NH_3$ ice with an estimated thickness of 9 monolayers without (0 μC/$cm^2$) and after electron exposure of 500 μC/$cm^2$ at $E_0$ = 20 eV. Formation of $N_2H_4$ at 20 eV is deduced from the appearance of a desorption signal around 185 K after exposure. All curves are shown with identical magnification. Ticks on the vertical axis indicate zero intensity for each curve.

**Formation of $N_2H_4$ in $NH_3$ ice**

$N_2H_4$ results from the recombination of two $NH_2^•$ radicals. The formation of $N_2H_4$ in $NH_3$ ice thus gives evidence at which electron energies $NH_2^•$ radicals are efficiently produced. To reveal that $N_2H_4$ was indeed formed, TDS curves were recorded at m/z values of 29 to 32 before and after irradiation of $NH_3$ ice with an $E_0$ of 20 eV and an electron exposure of 500 μC/$cm^2$ (Fig. 1). These m/z values dominate the mass spectrum of $N_2H_4$ [33] but are absent from TDS of $NH_3$ without irradiation (Fig. 1, bottom curve for each m/z value). After irradiation, desorption peaks are centered around 185 K for all four m/z values (Fig. 1, top curve for each m/z value). The ratio of the integrated TDS signals for m/z 31 and m/z 32 amounts to 44:100 which is close to the intensity ratio of 47:100 of the two signals in the mass spectrum [33]. This clearly supports that $N_2H_4$ was indeed formed in line with earlier results obtained after electron irradiation of $NH_3$ or $ND_3$ at both 1 keV and low energies [28] as well as after photolysis with energies below 7.4 eV [29].

The characteristic m/z 32 signal was used to monitor the formation of $N_2H_4$ as function of electron exposure (Fig. 2a) and electron energy (Fig. 2b). To this end, the TDS signals were integrated in the temperature range from 160 K to 300 K. The peak area and thus the yield of $N_2H_4$ increased linearly for electron exposures up to at least 50 μC/$cm^2$ at an $E_0$ of 20 eV (Fig. 2a). As the m/z 32 signal is unique to $N_2H_4$ in the experiments on pure $NH_3$ ice layers, it does not overlap with other signals. Therefore, a particularly low exposure of 50 μC/$cm^2$, well below the saturation level of the yield at 20 eV was chosen to monitor the energy dependence of the $N_2H_4$ production (Fig. 2b). The contribution of the baseline noise in the TDS data was evaluated by performing the integration of the m/z 32 curves on several non-irradiated $NH_3$ ices. The thus obtained average and its standard deviation is represented by the horizontal solid and dashed

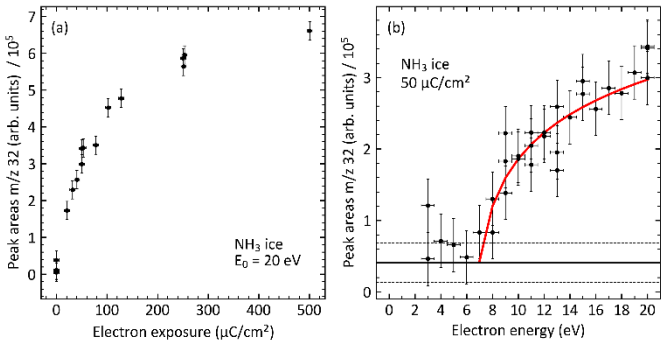


**Fig. 2.** Areas of the desorption peak ascribed to $N_2H_4$ within the m/z 32 TDS curve as obtained after electron irradiation of $NH_3$ ice with an estimated thickness of 9 monolayers. Integration was performed between 160 K and 300 K. (a) Dependence of the peak area on electron exposure at $E_0$ = 20 eV. (b) Dependence of the peak area on incident electron energy $E_0$ after irradiation with 50 μC/cm². The vertical solid and dashed lines represent the average integral obtained from several non-irradiated $NH_3$ ices and its standard deviation. The red line serves as a guide to the eye.

lines in Fig. 2b. The integrals obtained after electron irradiation lie systematically above this average for the non-irradiated ices even at low $E_0$. This is unexpected at $E_0$ below 5 eV which lies below the lowest DEA process [44]. However, the data points at 3 eV reveal a significant scatter in the results. This effect is rationalized by inspection of the raw data obtained after irradiation which shows that the baseline is not flat in all cases (ESI,† Fig. S5). In contrast and as visualized by the red line that has been drawn as a guide to the eye in Fig. 2b, the yield of $N_2H_4$ lies above the low-energy scatter and increases steadily with increasing $E_0$ above 8 eV. Based on this analysis, we deduce from the present data a threshold for formation of $N_2H_4$ of roughly 8 eV. Above this $E_0$, electron irradiation thus produces a sufficiently large amount of $NH_2^\bullet$ radicals to allow for an efficient recombination to $N_2H_4$.

The electron energy-dependent yield shown in Fig. 2b argues against a dominant contribution of DEA as an initiating step in the formation of $N_2H_4$. In the gas phase, DEA to $NH_3$ leads to release of H and $NH_2^-$ or alternatively to $H^-$ and $NH_2^\bullet$ radicals at $E_0$ around 5.5 eV and 10.5 eV [45,46]. Electron-stimulated desorption (ESD) of $D^-$ from condensed layers of $ND_3$, which must again be accompanied by release of $ND_2^\bullet$ radicals, was observed around 6.5 eV and around 8.5-9 eV [44]. In contrast, the energy-dependent yield of $N_2H_4$ obtained here (Fig. 2b) does not show maxima at these $E_0$ thus ruling out a dominant contribution of DEA.

The thermodynamic threshold for ND of $NH_3$ by N-H bond dissociation in the ground state is 4.6 eV [47]. A more conceivable ND pathway results from electronic excitation which has a threshold of 5.4 eV [48]. The previously observed formation of $N_2D_4$ in condensed $ND_3$ as a result of photolysis with energy below 7.4 eV [29] supports that ND is energetically accessible at such low energies. However, product yields in the present experiment are within the noise level in this energy range (Fig. 2b) suggesting that ND is also not a dominant reaction pathway towards the electron-induced formation of $N_2H_4$.

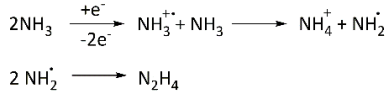


**Scheme 3.** Electron-induced formation of $NH_2^\bullet$ radicals via EI of condensed $NH_3$ and recombination to hydrazine.

The third possible fragmentation mechanism is initiated by ionization of $NH_3$. The EI threshold of $NH_3$ in the gas phase is 10.07 eV [38] while DI sets in only around 15 eV [49]. This is too high to explain the threshold for formation of $N_2H_4$ of 8 eV as observed herein (Fig 2b). However, in the condensed phase, EI triggers proton transfer leading to $NH_4^+$ and $NH_2^\bullet$ radicals [27] (Scheme 3). In fact, the lowest ionization energy of liquid $NH_3$ has been obtained from photoelectron experiments on $NH_3$ droplets that show a band with maximum at 9.1 eV and onset around 8 eV [50], in excellent agreement with the onset of $N_2H_4$ formation observed herein. Therefore, we conclude that EI is the most efficient electron-induced process with respect to formation of $NH_2^\bullet$ radicals in condensed $NH_3$ and dominates the yield of the recombination product $N_2H_4$.

### Formation of C4 hydrocarbons in $C_2H_4$ and $C_2H_6$ ices

Reactive species produced by electron interactions with hydrocarbon molecules typically undergo crosslinking or oligomerization reactions [21,30]. The formation of larger hydrocarbon molecules thus gives evidence that $C_2H_4$ and $C_2H_6$ are converted to reactive species as result of electron irradiation. C4 hydrocarbons are expected as most immediate products, but larger oligomers are also anticipated. Therefore, TDS experiments with $C_2H_4$ and $C_2H_6$ ices were performed after electron irradiation to identify such products and thus to reveal the electron-induced formation of reactive species.

The different isomers of butane ($C_4H_{10}$) and butene ($C_4H_8$) as well as butadiene ($C_4H_6$) are likely C4 products. According to data summarized in Table 1, m/z 43 is the base MS signal (100%) of butane isomers and unique to these. m/z 41 is the base signal of all butene isomers but also a medium to intense signal of butane isomers (29-38%). m/z 39 is the base signal of 1,3-butadiene but also appears with medium intensity in the MS of the different butane (14-17%) and butene (31-51%) isomers as well as in 1,2-butadiene (42%). In the signal group of the parent cations, m/z 58 again represents uniquely the butane isomers. Here, however, m/z 56 and 54 also reflect predominantly the butene and butadiene isomers, respectively. Fig. 3 shows TDS data recorded at these characteristic m/z ratios from $C_2H_6$ and $C_2H_4$ ices after an electron exposure of 250 μC/cm² at 15 eV. While the reactants $C_2H_6$ and $C_2H_4$ desorb around 55-60 K (see below and [24]), all curves reveal desorption peaks around 120 K, in close agreement with desorption signals that were reported earlier with maxima at 115 K for butane, 120 K for butene isomers, and at slightly higher temperature for butadiene [24]. This gives evidence that C4 hydrocarbons are indeed formed upon electron irradiation of condensed layers of $C_2H_6$ and $C_2H_4$.

**Table 1.** MS intensities for C4 hydrocarbons [33] and calculated total ionization cross sections (TICS) as well as partial ionization cross sections (PICS) derived from the TICS and the MS intensities as described in the experimental section.

| | TICS/Å² (70 eV) | MS intensities (and PICS/Å²) at m/z | | | | | |
|---|---|---|---|---|---|---|---|
| | | 58 | 56 | 54 | 43 | 41 | 39 |
| $C_4H_{10}$ | | | | | | | |
| n-butane | 12.0 | 12 (0.47) | <1 | <1 | 100 (3.85) | 29 | 14 |
| isobutane | 11.9 | 3 (0.12) | <1 | <1 | 100 (4.66) | 38 | 17 |
| $C_4H_8$ | | | | | | | |
| 1-butene | 10.4 | <1 | 39 (1.32) | 2 | <1 | 100 (3.39) | 34 |
| 2-butene | 10.5 | | 53 (1.23) | 4 | | 100 (2.30) | 51 |
| 2-butene (E) | 10.5 | <1 | 48 (1.44) | 4 | <1 | 100 (3.01) | 36 |
| 2-butene (Z) | 10.5 | <1 | 57 (1.83) | 4 | <1 | 100 (3.20) | 31 |
| isobutene | 10.5 | <1 | 45 (1.47) | 2 | <1 | 100 (3.30) | 45 |
| $C_4H_6$ | | | | | | | |
| 1,3-butadiene | 9.2 | | <1 | 95 (1.89) | | <1 | 100 (1.99) |
| 1,2-butadiene | 10.1 | | <1 | 100 (2.59) | | <1 | 42 (1.10) |

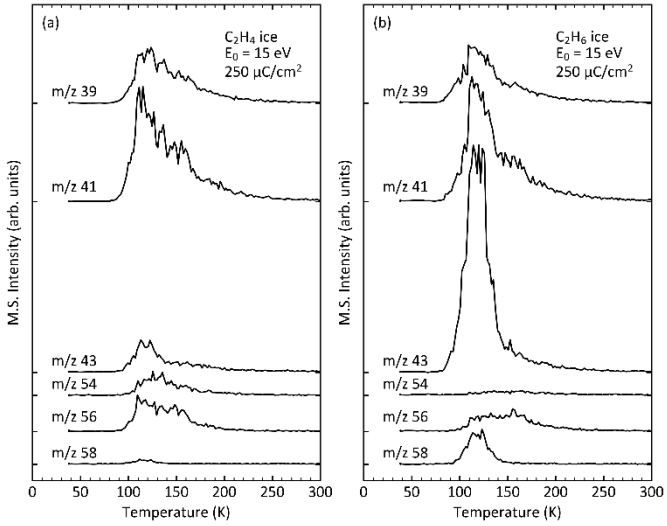


**Fig. 3.** Thermal desorption spectra obtained for m/z 39, 41, and 43 (base peaks of C4 hydrocarbons) as well as m/z 54, 56 and 58 (parent signals of C4 hydrocarbons) from (a) $C_2H_4$ and (b) $C_2H_6$ ices with an estimated thickness of 10 monolayers after an electron exposure of 250 μC/cm² at $E_0$ = 15 eV. Formation of C4 hydrocarbons is deduced from the appearance of a desorption signal around 120 K after exposure. Overlapping desorption peaks at higher temperature indicate that larger hydrocarbons are also formed. All curves are shown with identical magnification. Ticks on the vertical axis indicate zero intensity for each curve.

The TDS data obtained from $C_2H_4$ (Fig. 3a) and $C_2H_6$ (Fig. 3b) ices after electron irradiation at $E_0$ = 15 eV differ most noticeably from each other with respect to the intensity of the desorption signals in the m/z 43 and m/z 58 curves characteristic of butane isomers. These signals are much more intense in the case of $C_2H_6$. Here, a rough estimate of the relative amounts of butanes, butenes, and butadienes can be obtained from the ratio of the desorption peak heights for m/z 43, 41, and 39, which is about 4:2:1. Considering the contributions of butane isomers to the m/z 41 and 39 signals as well as of the different butenes to m/z 39, relative desorption peak heights for butane, butene, and butadiene isomers, respectively, can be derived. Correcting these intensities by the partial ionization cross sections (PICS) listed in Table 1 and focusing again on an estimate of the maximum possible result for butene and butadiene isomers, we arrive at relative amounts of butanes:butenes:butadienes of about 12:6:1. This represents an upper limit for the relative product yield of the unsaturated compounds. According to this quick estimate, saturated compounds are most abundant among the C4 hydrocarbons formed upon electron exposure of $C_2H_6$ ice. For $C_2H_4$, in contrast, the desorption signals at m/z 43 and 58 are less intense than the signals obtained at m/z 41 and 39 and m/z 56 and 54, respectively. This indicates that electron irradiation of $C_2H_4$ ice yields predominantly unsaturated C4 products, in line with the lower hydrogen content of the reactant.

The desorption peak of the C4 hydrocarbons overlaps with a further desorption signal around 150 K. This points to the formation of longer hydrocarbons such as C6 or even larger products. Their contribution to the TDS signals in the m/z 58 and, in particular, in the m/z 43 curve is small compared to the other m/z curves (Fig. 3). As the MS data of saturated C6 hydrocarbons reveal intense m/z 43 signals (ESI,† Table S1), we can conclude that the majority of the larger products is unsaturated. In contrast, the desorption signals around 150 K overlap with the C4 desorption peaks in the m/z 41, 39, 56, and 54 TDS data in line with the presence of these fragments in the MS of C6 hydrocarbons (ESI,† Table S1). In general, the exact position of a desorption signal can shift depending on the coverage if products are present in submonolayer quantities [51]. This condition applies to the small exposures applied herein [27,52,53] and is exemplified here by TDS data for m/z 41 obtained from $C_2H_4$ ice after an electron exposure of 250 μC/cm² at 10 eV and 15 eV (Fig. 4). The data recorded at 10 eV show a desorption peak with maximum around 125 K. At 15 eV, the desorption signal is more intense with maximum located at slightly lower temperature in line with an increased amount of product. In contrast, the desorption signal of larger products around 150 K is still very weak after electron exposure at 10 eV but present as an intense shoulder at 15 eV indicating that the contribution of larger hydrocarbons increases with increasing electron energy. Because of these varying contributions of C4 and larger hydrocarbons and also because of the strong overlap of the desorption signals relating to C4 and larger products, the contributions of different products cannot easily be separated. Therefore, we do not attempt to quantify the desorption signal relating to C4 products alone. Considering the margins of error of the estimate described above, we also do not derive relative amounts of butane and butene isomers as well as of butadiene. Instead, we use in the following the total integrated desorption signals for the different m/z values that include contributions of both C4 and larger hydrocarbons to monitor the product formation as function of electron exposure (Fig. 5) and to represent the dependence of the electron-driven reactivity of $C_2H_4$ and $C_2H_6$ on $E_0$ (Fig. 6).

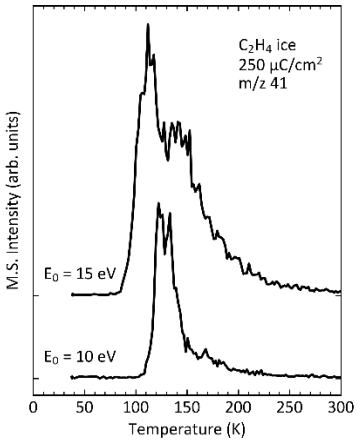


**Fig. 4.** Thermal desorption spectra obtained for m/z 41 from $C_2H_4$ ices with an estimated thickness of 10 monolayers after an electron exposure of 250 μC/cm² at $E_0$ = 15 eV (top) and 10 eV (bottom). Both curves are shown with identical magnification. Ticks on the vertical axis indicate zero intensity for each curve.

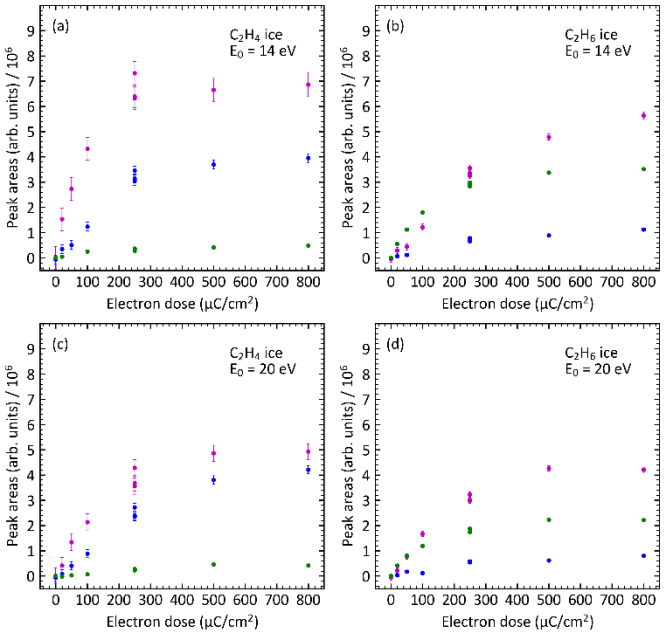


**Fig. 5.** Desorption peak areas within the TDS curves recorded at m/z 58 (green), 56 (magenta), and 54 (blue) from (a,c) $C_2H_4$ and (b,d) $C_2H_6$ ices with an estimated thickness of 10 monolayers after increasing electron exposure at $E_0$ = 14 eV (top) and $E_0$ = 20 eV (bottom). Integration was performed in the 70 to 320 K range.

Fig. 5 shows the dependence of the desorption peak areas on electron exposure of $C_2H_4$ and $C_2H_6$ ices recorded at m/z 58, 56, and 54. For both compounds, the peak areas obtained after irradiation with an $E_0$ of 20 eV increase linearly at least up to an exposure of 100 μC/cm² and begin to saturate at 250 μC/cm² (Fig. 5c,d). However, the increase is roughly linear up to 250 μC/cm² at 14 eV (Fig. 5a,b). To obtain a good signal-to-noise ratio, 250 μC/cm² were also applied to study the dependence of the integrated desorption signals on $E_0$ for both the base peaks at m/z 43, 41, and 39 (Fig. 6a,b) and the parent signals m/z 58, 56, and 54 (Fig. 6c,d) of C4 hydrocarbons. For both $C_2H_4$ and $C_2H_6$ ices, production of larger hydrocarbons shows a threshold behavior. This threshold is located between 8 and 9 eV in the case of $C_2H_4$ (Fig. 6a) and around 10 eV in the case of $C_2H_6$ (Fig. 6b). This difference and its implications regarding the most conceivable electron-molecule interactions for initiating product formation are discussed next.

DEA to $C_2H_4$ in the gas phase has been observed with maxima around 7.5 eV, 8.8 eV, and 10.5 eV, of which the last is most intense [54,55]. In the condensed phase, DEA has been detected via ESD of anions [56]. Among those, $H^-$ has an onset as low as 6 eV and maximum around 9 eV. DEA to $C_2H_6$ in the gas phase appears with maximum at 9.2 eV [55] while ESD from condensed $C_2H_6$ has an onset slightly below 8 eV and a maximum around 10 eV [56]. Radical fragments released by DEA can, in principle, activate further molecules to initiate the formation of larger hydrocarbons. However, product formation from both $C_2H_4$ and $C_2H_6$ as observed herein (Fig. 6) sets in at $E_0$ that are about 2 eV above the threshold for ESD [56]. While we cannot exclude that DEA contributes to a minor extent at the threshold of product formation, the lack of product formation between 6 and 8 eV in $C_2H_4$ and between 8 and 10 eV from $C_2H_6$ as well as the absence of a resonant structure in the product yield around 10 eV (Fig. 6) argues against a dominant role of DEA in the formation of larger hydrocarbons. It is tempting to relate the shift between the onset of ESD [56] and the onset of C4 production observed herein to additional activation barriers for reactions of radical fragments with $C_2H_4$. However, barriers for H abstraction

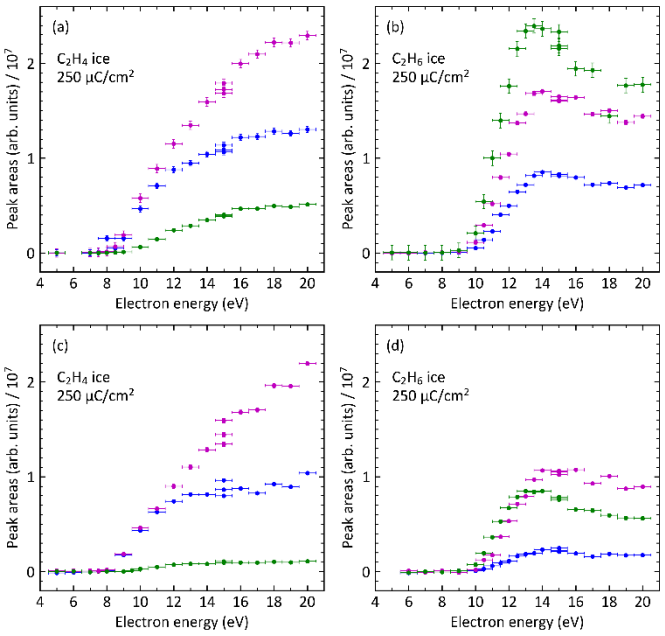


**Fig. 6.** Desorption peak areas as function of $E_0$ within the TDS curves recorded at (a,b) m/z 43 (green), 41 (magenta), and 39 (blue) and at (c,d) m/z 58 (green), 56 (magenta), and 54 (blue) obtained from (a,c) $C_2H_4$ and (b,d) $C_2H_6$ ices with an estimated thickness of 10 monolayers after electron exposures of 250 μC/cm². Integration was performed in the 70 to 320 K range.

from hydrocarbons by hydrocarbon radicals have been calculated as less than 0.8 eV [57,58] and thus cannot account for the shift of 2 eV.

ND reactions initiated by electronic excitation in $C_2H_4$ ice have been reported for photon energies above a threshold of 5.9 eV leading to $C_2H_2$ via loss of $H_2$ [59]. Electron impact excitation can populate the

even lower lying triplet $^3\pi\pi^*$ state at 3.5-5 eV [60]. However, no reports of reactions in this energy range have been brought forward to the best of our knowledge in accord with the lack of product formation below 8 eV in pure condensed $C_2H_4$ as observed in the present study. In $C_2H_6$, ND following photoabsorption, i.e. population of excited singlet states, has only been reported for photon energies above 10 eV [61]. Electronic excitation is possible at energies above 7 eV starting again with a low-lying triplet excited state [62] and may lead to various dissociative decay channels and thus reactive radical fragments [63]. The apparent lack of C4 product formation in the present experiments suggests that these fragments do not efficiently lead to product formation in condensed $C_2H_6$. Overall, the present data do not provide evidence for a dominant role of ND to the formation of larger hydrocarbons upon electron irradiation of $C_2H_4$ and $C_2H_4$ ice.

EI of $C_2H_4$ is anticipated to initiate a cationic oligomerization (Scheme 4) [30]. This reaction is the most conceivable explanation for the formation of larger hydrocarbons despite the fact that the threshold for formation of larger hydrocarbons from $C_2H_4$ lies considerably below the gas phase ionization energy of $C_2H_4$ of 10.5 eV [38]. This conclusion is based on the observation that the difference between this energy and the threshold between 8 and 9 eV for formation of C4 products is similar to the gas-to-solid shift of the vertical ionization energy reported previously as 1.7 eV [64]. The gas phase thresholds for EI (11.5 eV [38]) and DI (near 12 eV for $C_2H_4^{\bullet+}$ and $C_2H_5^+$, and others above [65]) of $C_2H_6$ again appear too high to explain the onset of product formation at 10 eV seen herein. A gas-to-solid shift of the ionization energy has not been reported for $C_2H_6$. Considering, however, the shifts of the vertical ionization energy reported as 1.7 eV for $C_2H_4$ and 1.2 eV for $CH_4$ [64]. and assuming a similar stabilization for $C_2H_6$, the threshold for EI would decrease to somewhere between 10 eV and 10.5 eV in $C_2H_6$ ice, near the onset of C4 product formation seen in the present study.

The electron-driven formation of C4 products has been detected before in MS experiments with electron ionization at 13 eV [66]. Later, the formation of butane from $C_2H_6$ was investigated by MS of $H_2$ gas with an admixture of $C_2H_6$ at temperatures between 128 K and 625 K [67] and by infrared spectroscopy of He droplets (0.4 K) doped with $C_2H_6$ and irradiated with 100 eV electrons [68]. The former work [67] detected $C_4H_{11}^+$ and its decay to $C_4H_9^+$ and monitored the temperature dependence of the reaction. A previous radiolysis study [69] also suggested the formation of covalently bound adducts of $C_2H_5^+$ and $C_2H_6$ and their decay by loss of $H_2$. In contrast, the He droplet study [68] gave only evidence of clusters of the cation fragments with neutral $C_2H_6$. Our study confirms the formation of covalent dimers. As a tentative explanation for the discrepancy with the He droplet study [68], we may propose that the temperature of the He droplets was too low to enable the reaction. At 128 K, the reaction of $C_2H_5^+$ with $C_2H_6$ was observed to proceed rapidly yielding $C_4H_{11}^+$ as the major product [67]. It was proposed that this product results from insertion of the cation into a C-H bond of a neutral $C_2H_6$ and is stabilized by third-body collisions. For $C_2H_4^{\bullet+}$, which is the dominant fragment within the MS of $C_2H_6$ [33], a similar insertion reaction was proposed to lead to formation of the n-butane radical cation [67]. These reactions are summarized in Scheme 5.

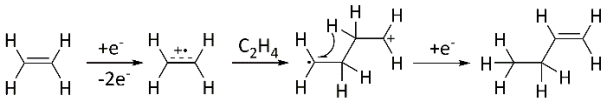


**Scheme 4.** Cationic oligomerization of $C_2H_4$ induced by EI [30].

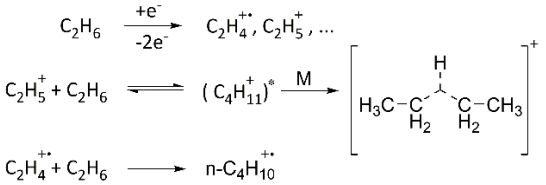


**Scheme 5.** Mechanism for formation of cationic $C_4$ products from $C_2H_6$ following EI at low temperature as proposed earlier [67]. The reaction proceeds by insertion of cationic fragments of $C_2H_6$ resulting from EI into C-H bonds of a neutral $C_2H_6$. The cationic product is stabilized by a collision with and energy transfer to a spectator molecule M.

Neutralization by recombination with a thermal electron within a $C_2H_6$ ice layer and dissipation of excess energy into the ice most likely converts the cationic C4 species to the C4 hydrocarbons that are observed in Fig. 3. Overall, this review of earlier work together with the thresholds for formation of C4 and larger hydrocarbons observed in the present study suggest EI as the most likely mechanism to initiate the reactions that lead to formation of larger hydrocarbons in both $C_2H_4$ and $C_2H_6$ ices as observed herein.

### Formation of ethylamine and C4 hydrocarbons in mixed $C_2H_4$:$NH_3$ and $C_2H_6$:$NH_3$ ices

The MS of ethylamine exhibits the parent ion at m/z 45 and the base signal at m/z 30 with relative intensities of 1:5 [33]. The former signal is absent in the MS of hydrocarbons and thus unique to ethylamine. Therefore, the electron-induced formation of ethylamine was monitored using TDS signals at m/z 45. However, to identify the product after electron irradiation of mixed $C_2H_4$:$NH_3$ and $C_2H_6$:$NH_3$ ices, TDS curves were first recorded at both m/z 45 and 30. For easier visualization, Fig. 7 shows representative TDS data obtained after an electron exposure of 800 μC/cm² at 15 eV. Both mixed ices show desorption signals between 140 K and 200 K. In the case of $C_2H_6$:$NH_3$ ice, the m/z 30 signal is superimposed on the intense tail of the $C_2H_6$ desorption peak which leads to a strong slope of the background. Nonetheless, in both cases the scaling factors applied to the TDS curves suggest that the relative intensities of the m/z 45 and 30 desorption signal match roughly the MS data [33] giving evidence that ethylamine is indeed formed. The signals of ethylamine are smaller but still clearly visible for a shorter exposure of 250 μC/cm² but somewhat shifted to higher temperature as anticipated for product amounts within the submonolayer regime (ESI,† Figs. S6 and S7).

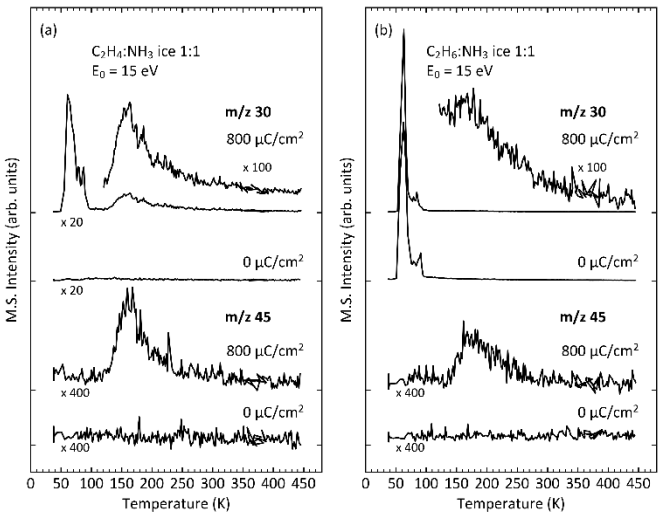


**Fig. 7.** Thermal desorption spectra obtained for m/z 30 (base peak of ethylamine) and m/z 45 (parent signal of ethylamine) from (a) $C_2H_6$:$NH_3$ and (b) $C_2H_4$:$NH_3$ ices (1:1) with an estimated thickness of 12 monolayers without (denoted as 0 μC/cm²) and after an electron exposure of 800 μC/cm² at $E_0$ = 15 eV. Formation of ethylamine is deduced from the appearance of a desorption signal between 140 K and 200 K after exposure. The vertical axes in both plots are shown with identical magnification with ticks indicating zero intensity for each curve.

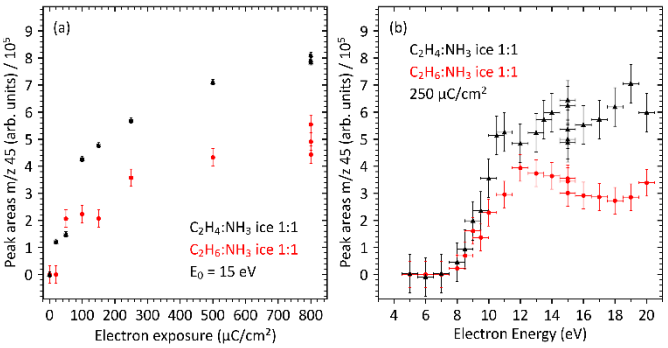


**Fig. 8.** Areas of the desorption peak ascribed to ethylamine within the m/z 45 TDS curve as obtained after electron irradiation of $C_2H_4$:$NH_3$ and $C_2H_6$:$NH_3$ mixed ices (1:1) with an estimated thickness of 12 monolayers. Integration was performed in the 130 K to 315 K range. (a) Dependence of the peak area on electron exposure at $E_0$ = 15 eV. (b) Dependence the peak area on incident electron energy $E_0$ after irradiation with 250 μC/cm².

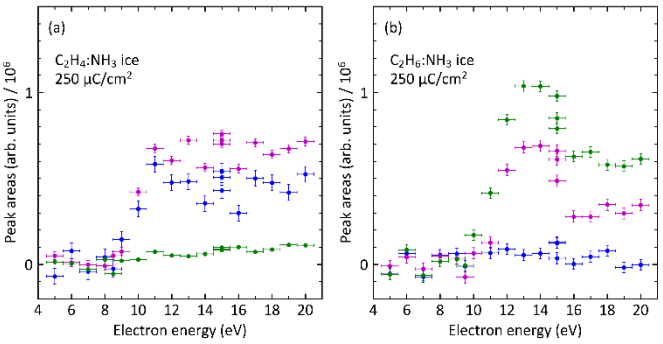


**Fig. 9.** Areas of the desorption peak ascribed to C4 and larger hydrocarbons within the TDS curves recorded at m/z 58 (green), 56 (magenta), and 54 (blue) as function of $E_0$ obtained from (a) $C_2H_4$:$NH_3$ and (b) $C_2H_6$:$NH_3$ mixed ices (1:1) with an estimated thickness of 12 monolayers after electron exposures of 250 μC/cm². Integration was performed in the 110 K to 215 K range.

In both $C_2H_4$:$NH_3$ and $C_2H_6$:$NH_3$ ices (1:1), the formation of ethylamine was first monitored as function of electron exposure at 15 eV (Fig. 8a) As for the pure hydrocarbons, product formation starts to saturate above 100 μC/cm². However, for the sake of a better visualization of the energetic threshold, the product formation as function of $E_0$ was again measured for exposures of 250 μC/cm² (Fig. 8b). Overall, Fig. 8 reveals that electron irradiation produces ethylamine not only in mixed $C_2H_4$:$NH_3$ ice as reported before [23,24] but also, with similar efficiency, in $C_2H_6$:$NH_3$ ice. This result is surprising because previous attempts to identify ethylamine in $C_2H_6$:$NH_3$ ice were not successful [23]. This discrepancy can, however, be rationalized by considering the overlap of the dominant m/z 30 ethylamine TDS signal with the desorption peak of $C_2H_6$ (ESI,† Fig S7). Furthermore, the ice in the earlier study was prepared by simply leaking a 1:1 gas mixture [23]. This must have translated into an ice that was less rich in $NH_3$ than used in the present experiments (see Section 2). This would have produced a lower yield of ethylamine which, in consequence, remained unnoticed.

Notably, the threshold for formation of ethylamine is located around 8 eV in both $C_2H_4$:$NH_3$ and $C_2H_6$:$NH_3$ ices (Fig. 8b). In contrast, the thresholds for formation of C4 and larger hydrocarbons and thus for direct production of reactive species from $C_2H_4$ and $C_2H_6$ also differ from each other in the mixed ices (Fig. 9). The yield of larger hydrocarbons in the mixed ices is lower than in pure $C_2H_4$ and $C_2H_6$ (see Fig. 6) which is rationalized by the lower amount of hydrocarbon reactant in the mixture as well as by concurrent reactions such as the formation of ethylamine or the deactivation of reactive intermediates by reaction with hydrogen released upon electron-initiated fragmentation of $NH_3$ (see below). Nonetheless, Fig. 9 reveals the threshold for formation of larger hydrocarbons from $C_2H_4$:$NH_3$ ice in the 8-9 eV range while the threshold is again located around 10 eV in the case of $C_2H_6$:$NH_3$ ice. This indicates that the direct activation of the hydrocarbon by the impinging electron is not decisive for the threshold of ethylamine formation.

As the key observation, the threshold of roughly 8 eV for the production of $N_2H_4$ from $NH_3$ by electron ionization (Fig. 2) coincides with the threshold for production of ethylamine in the mixed ices (Fig. 8). Formation of $N_2H_4$ indicates that the density of $NH_2^\bullet$ radical intermediates is high enough to allow for an encounter of two such species. As described in detail previously [27], $NH_2^\bullet$ released upon electron ionization of $NH_3$ and subsequent proton transfer to a second $NH_3$ can directly add to one of the C atoms involved in the double bond of $C_2H_4$. The hydrogen bond network facilitates migration of a hydrogen to the resulting radical site on the second C atom leading to the formation of ethylamine (Scheme 2). This reaction is also conceivable in mixed $C_2H_6$:$NH_3$ ices as soon as $C_2H_6$ is converted to $C_2H_4$ by electron-induced loss of $H_2$. ESD of $H_2$ has been observed previously from alkanethiol SAMs [70] with onset as low as 5 eV and thus considerably below the threshold for formation of ethylamine as seen herein. The reactivity at these low energies was ascribed to electronic excitation processes and, although dissociation of a single C-H bond was also not ruled out, it was concluded that $H_2$ was released as consequence of direct molecular

elimination [70]. This conclusion is in line with studies that revealed the formation of CC double bonds within such SAMs as a result of electron irradiation at 50 eV [71]. The present experiments do not allow us to quantify the analogous conversion of $C_2H_6$ to $C_2H_4$ via loss of $H_2$ because both the mass pattern and the desorption temperatures of $C_2H_6$ to $C_2H_4$ overlap strongly so that small quantities of $C_2H_4$ would be masked by the majority species $C_2H_6$. However, this reaction is conceivable. Electronic excitation of $C_2H_6$ in the energy range between 7 and 8 eV can proceed under electron irradiation [62] and dissociative reaction channels including loss of $H_2$ are accessible from electronically excited $C_2H_6$ [63]. However, the lack of C4 and larger products in pure $C_2H_6$ ice below electron energies of 10 eV as observed herein (Figs. 6,9) suggests that this reaction only leads to minor quantities of $C_2H_4$ under the present conditions. Also, a maximum of 25% of the initial quantity of $C_2H_6$ has undergone a reaction after an exposure of 250 μC/cm$^2$ at 15 eV and even less at 10 eV (ESI,† Fig. S8). Assuming a quantitative conversion to $C_2H_4$, this would account for about 1/3 of the amount of ethylamine actually produced at 15 eV in the $C_2H_6$:$NH_3$ mixed ice as seen in Fig. 8a. Therefore, we conclude that the amount of $C_2H_4$ accumulated upon electron irradiation in $C_2H_6$ or $C_2H_6$:$NH_3$ mixed ice is too small to explain the yields of ethylamine as observed in Fig 7 and Fig. 8.

As an additional reaction pathway to the formation of ethylamine in $C_2H_6$:$NH_3$ ice, we propose a direct reaction of $NH_2^\bullet$ radicals with $C_2H_6$. As for the reaction with $C_2H_4$ described above, the onset of ethylamine production at 8 eV suggests that the amount of available $NH_2^\bullet$ also limits the rate of ethylamine formation in $C_2H_6$:$NH_3$ ice. $NH_2^\bullet$ radicals have been reported to activate $C_2H_6$ with an activation barrier around 0.4 eV leading to formation of $C_2H_5^\bullet$ radicals and $NH_3$ [72]. The resulting $C_2H_5^\bullet$ radical can recombine with a further $NH_2^\bullet$. This scenario, which is summarized in Scheme 6, is likely given that formation of $N_2H_4$ also requires recombination of two $NH_2^\bullet$ radicals. Scheme 6 can thus rationalize the efficient formation of ethylamine as in $C_2H_6$:$NH_3$ ice (Fig. 8b). However, we also cannot rule out some contributions of reactions that proceed via electron-induced C-H bond cleavage and thus formation of $C_2H_5^\bullet$ radicals. Such species would be formed, for instance, when $H^-$ is released by DEA to $C_2H_6$ [56] but may also be produced by non-resonant processes at low energies [70]. $C_2H_5^\bullet$ radicals may then recombine with $NH_2^\bullet$ radicals as soon as the latter become available, i.e., starting with the observed threshold of 8 eV. The lack of production of larger hydrocarbons in this energy range does not fully argue against such a scenario because the recombination of two $C_2H_5^\bullet$ radicals may also be impeded by a lack of mobility. However, the lack of a pronounced maximum in the yield of ethylamine around 10 eV leads us to conclude that such resonant processes are not the dominant factor for the production of ethylamine in $C_2H_6$:$NH_3$ ice.

$$C_2H_6 + \dot{N}H_2 \longrightarrow C_2\dot{H}_5 + NH_3$$

$$C_2\dot{H}_5 + \dot{N}H_2 \longrightarrow C_2H_5NH_2$$

**Scheme 6.** Proposed mechanism for the formation of ethylamine from mixtures of ethane and $NH_3$.

The relatively small difference between the efficiencies of ethylamine production from $C_2H_4$:$NH_3$ and $C_2H_6$:$NH_3$ may also relate to the fact that $C_2H_4$ can be reduced to $C_2H_6$ by hydrogen that is released during electron-induced dissociation of $NH_3$. This effect was observed in previous work on the electron-induced reactions between $C_2H_4$ and $NH_3$ [23,24,27] and is also seen in the TDS data recorded at m/z 30 from $C_2H_6$:$NH_3$ ice where a new desorption peak around 60 K range appears after electron exposure (Fig. 7). This reduction is a concurrent reaction to the hydroamination as proposed in Scheme 1 and Scheme 2 but can also counteract the degradation of saturated hydrocarbon chains by electron-induced loss of hydrogen [25]. The latter effect is also apparent from experiments on mixed ices prepared with increasing $NH_3$ content while the amount of hydrocarbon was kept constant (Fig. 10). For both mixed ices, the $NH_3$:hydrocarbon ratio was varied between 1:4 and 3.5:1. The quantity of $NH_3$ was thus increased by a factor of 12. However, the yield of ethylamine increased by a mere factor of three to five with the variation being slightly less pronounced in the case of the $C_2H_6$:$NH_3$ ices. At the same time, however, the yield of larger hydrocarbons, represented here by the desorption signal in m/z 54 in the case of the $C_2H_4$:$NH_3$ ice and m/z 58 for $C_2H_6$:$NH_3$ ice, dropped significantly with increasing amount of $NH_3$. This indicates that reactive species such as $C_2H_5^\bullet$ radicals are more rapidly deactivated by recombination with atomic $H^\bullet$ delivered by electron-induced dissociation of $NH_3$ and thus cannot recombine with other radicals to form larger compounds. This same reaction also counteracts the recombination of $C_2H_5^\bullet$ with $NH_2^\bullet$ or removes $C_2H_4$ to which $NH_2^\bullet$ could add as decisive reaction steps in the formation of ethylamine.

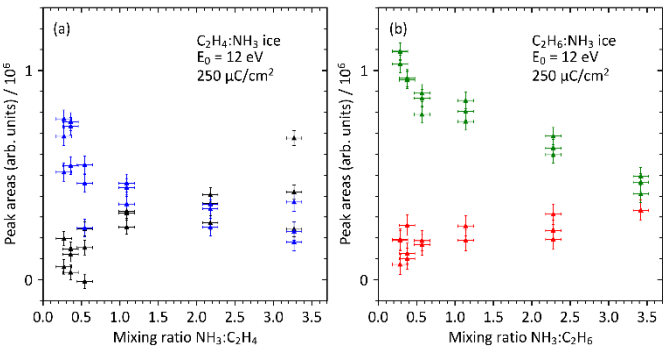


**Fig. 10.** Areas of the desorption peak ascribed to ethylamine within the m/z 45 (black/red) TDS curve and of C4 and larger hydrocarbons (m/z 54 (blue) and m/z 58 (green)) as obtained after electron irradiation with 250 μC/cm$^2$ at $E_0$ = 12 eV of (a) $C_2H_4$:$NH_3$ and (b) $C_2H_6$:$NH_3$ mixed ices with varying mixing ratio. In the experiments, the amount of hydrocarbon was kept constant at about 6 monolayers while the amount of $NH_3$ was increased leading to a total thickness ranging from roughly 8 to 24 monolayers for mixing ratios ranging from 1:4 to 3:1. Integration was performed between 130 and 270 K for ethylamine and between 110 and 215 K for the hydrocarbon products.

## 4. Conclusions

Previous studies on electron-induced hydroaminations [23-25] were guided by the hypothesis that unsaturated hydrocarbons are required for the reaction. Therefore, we anticipated that the amino functionalization of hydrocarbon materials via electron-

induced reactions in presence of $NH_3$ would be considerably more efficient for unsaturated reactants such as $C_2H_4$ than for saturated compounds, represented here by $C_2H_6$. This hypothesis was evaluated by monitoring the electron energy-dependent yield of ethylamine after electron irradiation of mixed $C_2H_4$:$NH_3$ and $C_2H_6$:$NH_3$ ices with the same composition and thickness. However, the results reveal a similar efficiency for formation of ethylamine for both ices and thus disprove our assumption. Comparison with the energy dependences of the $N_2H_4$ yield in pure $NH_3$ ice and of larger hydrocarbons in pure $C_2H_4$ and $C_2H_6$ ices together with a comprehensive survey of existing data on the electron-induced reactions of the reactants lead to the conclusion that, in both cases, the reaction is predominantly driven by electron ionization of $NH_3$. Ethylamine formation can be traced back to reaction of the resulting $NH_2^\bullet$ radicals with $C_2H_4$ and $C_2H_6$, respectively. Overall, the similar efficiency of ethylamine formation in $C_2H_4$:$NH_3$ and $C_2H_6$:$NH_3$ ices relates to (i) the existence of alternative reaction pathways for reaction of $NH_2^\bullet$ radicals with saturated and unsaturated CC bonds that lead to the same product and (ii) the fact that $C_2H_4$ and $C_2H_6$ can be converted to each other by electron-induced loss of $H_2$ and electron-induced reduction in presence of $NH_3$. Altogether, this rationalizes why the efficiency of ethylamine formation is similar for the two mixed ices studied herein and demonstrates that electron irradiation in presence of $NH_3$ is a more versatile tool for introducing nitrogen into carbonaceous materials than previously anticipated. This insight is not only relevant to the modification of materials but also helps to understand the chemistry involved in cosmic-ray induced processing of astrochemical ices.

## Author Contributions

Hannah Boeckers: Data curation (lead); formal analysis (lead); investigation (lead); software (equal); validation; visualization (lead); writing - review & editing (equal).
Martin Philipp Mues: Data curation ($NH_3$ ice); formal analysis ($NH_3$ ice); investigation ($NH_3$ ice); writing – review & editing (supporting).
Jan Hendrik Bredehöft: Software (equal); supervision (equal); visualization (supporting); writing - review & editing (equal).
Petra Swiderek: Conceptionalization; supervision (equal); writing – original draft preparation; writing – review & editing (equal).

## Conflicts of interest

There are no conflicts to declare.

## Notes and references


1 N. Kasera, P. Kolar and S. G. Hall, *Biochar*, 2022, **4**, 17. https://doi.org/10.1007/s42773-022-00145-2
2 T. Li, X. An and D. Fu, *Energy & Fuels*, 2023, **37**, 8160-8179. https://doi.org/10.1021/acs.energyfuels.3c00941
3 D. Villalgordo-Hernández, A. Grau-Atienza, A. A. García-Marín, E. V. Ramos-Fernández and J. Narciso, *Materials*, 2022, **15**, 2415. https://doi.org/10.3390/ma15072415
4 W. Al-Hajri, Y. De Luna and N. Bensalah, *Energy Technol.*, 2022, **10**, 2200498. https://doi.org/10.1002/ente.202200498
5 B. Petrovic, M. Gorbounov and S. Masoudi Soltani, *Carbon Capture Sci. Technol.*, 2022, **3**, 100045. https://doi.org/10.1016/j.ccst.2022.100045
6 Y. Shi, R. Ni and Y. Zhao, *Energy & Fuels*, 2023, **37**, 6365-6381. https://doi.org/10.1021/acs.energyfuels.3c00381
7 A. K. Sekizkardes, P. Wang, J. Hoffman, S. Budhathokia and D. Hopkinson, *Mater. Adv.*, 2022, **3**, 6668-6686. https://doi.org/10.1039/D2MA00235C
8 J. Hack, N. Maeda and D. M. Meier, *ACS Omega*, 2022, **7**, 39520-39530. https://doi.org/10.1021/acsomega.2c03385
9 H. Sun, Q. Zhang, T. Hagio, I. Ryoichi, L. Kong and L. Li, *Surf. Interfaces*, 2022, **33**, 102256. https://doi.org/10.1016/j.surfin.2022.102256
10 S. K. Dhilllon, P. P. Kundu and R. Jain, *Environ. Sci. Pollut. Res.*, 2023, **30**, 24815-24841. https://doi.org/10.1007/s11356-021-17529-9
11 B. Wu, H. Meng, D. M. Morales, F. Zeng, J. Zhu, B. Wang, M. Risch, Z. J. Xu and T. Petit, *Adv. Funct. Mater.*, 2022, **32**, 2204137. https://doi.org/10.1002/adfm.202204137
12 I. Ayyubov, E. Tálas, C. Berghian-Grosan, L. Románszki, I. Borbáth, Z. Pászti, Á. Szegedi, J. Mihály, A. Vulcu and A. Tompos, *React. Kinet. Mech. Catal.*, 2023, **136**, 125-147. https://doi.org/10.1007/s11144-022-02331-6
13 E. Dhandapani, S. Thangarasu, S. Ramesh, K. Ramesh, R. Vasudevan and N. Duraisamy, *J. Energy Storage*, 2022, **52**, 104937. https://doi.org/10.1016/j.est.2022.104937
14 A. R. Cherian, L. Benny, A. George, A. Varghese and G. Hegde, *J. Nanostructure Chem.*, 2022, **12**, 441-466. https://doi.org/10.1007/s40097-021-00426-5
15 H. Boeckers, P. Swiderek, M. Rohdenburg, *Nanomaterials*, 2022, **12**, 4455. https://doi.org/10.3390/nano12244455
16 K. Mainali, S. H. Mood, M. R. Pelaez-Samaniego, V. Sierra-Jimenez and M. Garcia-Perez, *Catal. Today*, 2023, **423**, 114248. https://doi.org/10.1016/j.cattod.2023.114248
17 V. M. Naik, S. V. Bhosalec and G. B. Kolekar, *Anal. Methods*, 2022, **14**, 877-891. https://doi.org/10.1039/D1AY02105B
18 N. Bouazizi, J. Vieillard, B. Samir and F. Le Derf, *Polymers*, 2022, **14**, 378. https://doi.org/10.3390/polym14030378
19 L. Lin, Y. Meng, T. Ju, S. Han, F. Meng, J. Li, Y. Du, M. Song, T. Lan and J. Jiang, *J. Environ. Manage.*, 2023, **325**, 116438. https://doi.org/10.1016/j.jenvman.2022.116438
20 S. M. George, B. Yoon and A. A. Dameron, *Acc. Chem. Res.*, 2009, **42**, 498-508. https://doi.org/10.1021/ar800105q
21 A. Turchanin and A. Gölzhäuser, *Prog. Surf. Sci.*, 2012, **87**, 108-162. https://doi.org/10.1016/j.progsurf.2012.05.001
22 A. Gölzhäuser, W. Eck, W. Geyer, V. Stadler, T. Weimann, P. Hinze and M. Grunze, *Adv. Mater.*, 2001, **13**, 806-809. https://doi.org/10.1002/1521-4095(200106)13:11%3C803::AID-ADMA806%3E3.0.CO;2-W
23 T. Hamann, E. Böhler and P. Swiderek, *Angew. Chem. Int. Ed.*, 2009, **48**, 4643-4645. https://doi.org/10.1002/anie.200901338
24 E. Böhler, J. H. Bredehöft and P. Swiderek, *J. Phys. Chem. C*, 2014, **118**, 6922-6933. https://doi.org/10.1021/jp501192v
25 T. Hamann, L. Kankate, E. Böhler, J. H. Bredehöft, F. Zhang, A. Gölzhäuser and P. Swiderek, *Langmuir*, 2012, **28**, 367-376. https://doi.org/10.1021/la2027219
26 F. Pohlki and S. Doye, *Chem. Soc. Rev.*, 2003, *32*, 104-114. https://doi.org/10.1039/B200386B
27 F. Schmidt, T. Borrmann, M. P. Mues, S. Benter, P. Swiderek and J. H. Bredehöft, *Atoms*, 2022, **10**, 25. https://doi.org/10.3390/atoms10010025
28 K. E. Shulenberger, J. L. Zhu, K. Tran, S. Abdullahi, C. Belvin, J. Lukens, Z. Peeler, E. Mullikin, H. M. Cumberbatch, J. Huang, K. Regovich, A. Zhou, L. Heller, M. Markovic, L. Gates, C. Buffo, R. Tano-Menka, C. R. Arumainayagam, E. Böhler, P. Swiderek, S. Esmaili, A. D. Bass, M. Huels and L. Sanche, *ACS*

*Earth Space Chem.*, 2019, **3**, 800-810. https://doi.org/10.1021/acsearthspacechem.8b00169
29 E. Mullikin, P. van Mulbregt, J. Perea, M. Kasule, J. Huang, C. Buffo, J. Campbell, L. Gates, H. M. Cumberbatch, Z. Peeler, H. Schneider, J. Lukens, S. T. Bao, R. Tano-Menka, S. Baniya, K. Cui, M. Thompson, A. Hay, L. Widdup, A. Caldwell-Overdier, J. Huang, M. C. Boyer, M. Rajappan, G. Echebiri and C. R. Arumainayagam, *ACS Earth Space Chem.*, 2018, **2**, 863-868. https://doi.org/10.1021/acsearthspacechem.8b00027
30 E. Böhler, J. Warneke and P. Swiderek, *Chem. Soc. Rev.*, 2013, **42**, 9219-9231. https://doi.org/10.1039/C3CS60180C
31 I. Ipoly, W. Michaelis and P. Swiderek, *Phys. Chem. Chem. Phys.*, 2007, **9**, 180-191. https://doi.org/10.1039/B612261B
32 C. Benndorf and T. E. Madey, *Surf. Sci.*, 1983, **135**, 164-183. https://doi.org/10.1016/0039-6028(83)90217-0
33 Stein, S. E. Mass Spectra. In NIST Chemistry WebBook; NIST Standard Reference Database Number 69; Linstrom, P. J., Mallard, W. G., Eds.; National Institute of Standards and Technology: Gaithersburg, MD; http://webbook.nist.gov (accessed 2023-09-11)
34 Y.-K. Kim and M. E. Rudd, *Phys. Rev. A: At., Mol., Opt. Phys.*, 1994, **50**, 3954-3967. https://doi.org/10.1103/PhysRevA.50.3954
35 W. Hwang, Y.-K. Kim and M. E. Rudd, *J. Chem. Phys.*, 1996, **104**, 2956-2966. https://doi.org/10.1063/1.471116
36 F. Neese, *WIREs Comput. Mol. Sci.*, 2012, **2**, 73-78. http://dx.doi.org/10.1002/wcms.81
37 F. Neese, F. Wennmohs, U. Becker and C. Riplinger, *J. Chem. Phys.*, 2020, **152**, 224108. https://doi.org/10.1063/5.0004608
38 Sharon G. Lias, "Ionization Energy Evaluation" in **NIST Chemistry WebBook, NIST Standard Reference Database Number 69**, Eds. P.J. Linstrom and W.G. Mallard, National Institute of Standards and Technology, Gaithersburg MD, 20899, https://doi.org/10.18434/T4D303, (retrieved September 21, 2023).
39 Sharon G. Lias, Rhoda D. Levin, and Sherif A. Kafafi, "Ion Energetics Data" in **NIST Chemistry WebBook, NIST Standard Reference Database Number 69**, Eds. P.J. Linstrom and W.G. Mallard, National Institute of Standards and Technology, Gaithersburg MD, 20899, https://doi.org/10.18434/T4D303, (retrieved September 21, 2023).
40 H. Nishimura and H. Tawara, *J. Phys. B: At. Mol. Opt. Phys.*, 1994, **27**, 2063-2074. DOI 10.1088/0953-4075/27/10/016
41 M. V. V. S. Rao and S. K. Srivastava, *J. Phys. B: At. Mol. Opt. Phys.* 1992, **25**, 2175-2187. DOI 10.1088/0953-4075/25/9/021
42 R. Rejoub, B.G. Lindsay and R.F. Stebbings, *J. Chem. Phys.* 2001, **115**, 5053-5058. https://doi.org/10.1063/1.1394748
43 J.A. Syage, *Aerospace Report* No. TR-94(4231)-3, 1994. https://apps.dtic.mil/sti/pdfs/ADA281248.pdf
44 M. Tronc, R. Azria, Y. Le Coat and E. Illenberger, *J. Phys. Chem.*, 1996, **100**, 14745-14750. https://doi.org/10.1021/jp9604305
45 M. Tronc, R. Azria and M. B. Arfa, *J. Phys. B: At. Mol. Opt. Phys.*, 1988, **21**, 2497-2506. **DOI** 10.1088/0953-4075/21/13/016
46 N. Barghava Ram and E. Krishnakumar, *J. Chem. Phys.*, 2012, **136**, 164308. https://doi.org/10.1063/1.4705358
47 S. Leach, H. W. Jochims and H. Baumgärtel, *Phys. Chem. Chem. Phys.*, 2005, **7**, 900–911. https://doi.org/10.1039/B409046M
48 M. Ben Arfa and M. Tronc, *Chem. Phys.*, 1991, **155**, 143-148. https://doi.org/10.1016/0301-0104(91)87014-M
49 Sharon G. Lias and Joel F. Liebman, "Ion Energetics Data" in **NIST Chemistry WebBook, NIST Standard Reference Database Number 69**, Eds. P.J. Linstrom and W.G. Mallard, National Institute of Standards and Technology, Gaithersburg MD, 20899, https://doi.org/10.18434/T4D303, (retrieved September 21, 2023).
50 T. Buttersack, P. E. Mason, R. S. McMullen, T. Martinek, K. Brezina, D. Hein, H. Ali, C. Kolbeck, C. Schewe, S. Malerz, B. Winter, R. Seidel, O. Marsalek, P. Jungwirth and S. E. Bradforth, *J. Am. Chem. Soc.*, 2019, **141**, 1838−1841. https://doi.org/10.1021/jacs.8b10942
51 E. Burean, I. Ipolyi, T. Hamann and P. Swiderek, *Int. J. Mass Spectrom.*, 2008, **277**, 215-219. https://doi.org/10.1016/j.ijms.2008.04.026
52 E. Burean and P. Swiderek, *Surf. Sci.*, 2008, **602**, 3194-3198. https://doi.org/10.1016/j.susc.2007.05.065
53 F. Schmidt, P. Swiderek and J. H. Bredehöft**,** *ASC Earth Space Chem.*, 2019, **3**, 1974-1986. https://doi.org/10.1021/acsearthspacechem.9b00168
54 E. Szymańska, N. J. Mason, E. Krishnakumar, C. Matias, A. Mauracher, P. Scheier and S. Denifl, *Int. J. Mass Spectrom.*, 2014, **365-366**, 356-364. https://doi.org/10.1016/j.ijms.2014.01.006
55 I. Cadez, S. Markelj and Z. Rupnik, *Eur. Phys. J. D*, 2012, **66**, 73. https://doi.org/10.1140/epjd/e2012-20651-2
56 P. Rowntree, L. Parenteau and L. Sanche, *J. Phys. Chem.*, 1991, **95**, 4902-4909. https://doi.org/10.1021/j100165a054
57 W. Klopper, R. A. Bachorz, D. P. Tew, J. Aguilera-Iparraguirre, Y. Carissan and C. Hättig, *J. Phys. Chem. A*, 2009, **113**, 11679-11684. https://doi.org/10.1021/jp902753s
58 M. Muszyńska, A. Ratkiewicz, L. K. Huynh and T. N. Truong, *J. Phys. Chem. A*, 2009, **113**, 8327-8336. https://doi.org/10.1021/jp903762x
59 J.-I. Lo, S.-L. Chou, Y.-C. Peng, H.-C. Lu and B.-M. Cheng, *Icarus*, 2018, **302**, 261-265. https://doi.org/10.1016/j.icarus.2017.11.015
60 T. P. T. Do, K. L. Nixon, M. Fuss, G. García, F. Blanco and M. J. Brunger, *J. Chem. Phys.*, 2012, **136**, 184313. https://doi.org/10.1063/1.4716184
61 K. Kameta, N. Kouchi, M. Ukai and Y. Hatano, *J. Electron Spectros. Relat. Phenomena*, 2002, **123**, 225-238. https://doi.org/10.1016/S0368-2048(02)00022-1
62 W.-Q. Xu, L.-Q. Xu, D.-G. Qi, T. Chen, Y.-W. Liu and L.-F. Zhu, *J. Chem. Phys.*, 2018, **148**, 144313. https://doi.org/10.1063/1.5021695
63 Y. Chang, J. Yang, Z. Chen, Z. Zhang, Y. Yu, Q. Li, Z. He, W. Zhang, G. Wu, R. A. Ingle, M. Bain, M. N. R. Ashfold, K. Yuan, X. Yang and C. S. Hansen, *Chem. Sci.*, 2020, **11**, 5089-5097. https://doi.org/10.1039/D0SC01746A
64 A. J. Yencha, H. Kubota, T. Fukuyama, T. Kondow and K. Kuchitsu, *J. Electron Spectrosc. Rel. Phenom.*, 1981, **23**, 431-440. https://doi.org/10.1016/0368-2048(81)85049-9
65 Sharon G. Lias, John E. Bartmess, Joel F. Liebman, John L. Holmes, Rhoda D. Levin, and W. Gary Mallard, "Ion Energetics Data" in **NIST Chemistry WebBook, NIST Standard Reference Database Number 69**, Eds. P.J. Linstrom and W.G. Mallard, National Institute of Standards and Technology, Gaithersburg MD, 20899, https://doi.org/10.18434/T4D303, (retrieved September 21, 2023).
66 R. C. Dunbar, J. Shen and G. A. Olah, *J. Chem. Phys.*, 1972, **56**, 3794-3798. https://doi.org/10.1063/1.1677781
67 K. Hiraoka and P. Kebarle, *Can. J. Chem.*, 1980, **58**, 2262-2270. https://cdnsciencepub.com/doi/pdf/10.1139/v80-364
68 S. Erukala, A. J. Feinberg, C. J. Moon, M. Y. Choi and A. F. Vilesov, *J. Chem. Phys.*, 2022, **156**, 204306. https://doi.org/10.1063/5.0091819
69 P. Ausloos, R. E. Rebbert and L. W. Sieck, *J. Chem. Phys.*, 1971, **54**, 2612-2618. https://doi.org/10.1063/1.1675220
70 M.A. Huels, P.-C. Dugal and L. Sanche, *J. Chem. Phys.*, 2003, **118**, 11168-11178. https://doi.org/10.1063/1.1574791

71 M. Zharnikov, W. Geyer, A. Gölzhäuser, S. Frey and M. Grunze, *Phys. Chem. Chem. Phys.*, 1999, **1**, 3163-3171. https://doi.org/10.1039/A902013F
72 K. Siddique, M. Altarawneh, J. Gore, P. R. Westmoreland and B. Z. Dlugogorski, Hydrogen abstraction from hydrocarbons by $NH_2$, *J. Phys. Chem. A*, 2017, **121**, 2221-2231. https://doi.org/10.1021/acs.jpca.6b12890